

PAPER

Electrically tunable magnetoplasmons in a monolayer of silicene or germanene

To cite this article: M Tahir and P Vasilopoulos 2015 *J. Phys.: Condens. Matter* **27** 075303

View the [article online](#) for updates and enhancements.

Related content

- [Dc and ac transport in silicene](#)
V Vargiamidis, P Vasilopoulos and G-Q Hai
- [The magnetic field particle-hole excitation spectrum in doped graphene and in a standard two-dimensional electron gas](#)
R Roldán, M O Goerbig and J-N Fuchs
- [Spin and valley filter in strain engineered silicene](#)
Wang Sa-Ke and Wang Jun

Electrically tunable magnetoplasmons in a monolayer of silicene or germanene

M Tahir and P Vasilopoulos

Department of Physics, Concordia University, Montreal, QC H3G 1M8, Canada

E-mail: m.tahir06@alumni.imperial.ac.uk

Received 29 August 2014, revised 29 December 2014

Accepted for publication 8 January 2015

Published 2 February 2015



Abstract

We theoretically study electrically tunable magnetoplasmons in a monolayer of silicene or germanene. We derive the dynamical response function and take into account the effects of strong spin-orbit coupling (SOC) and of an external electric field E_z perpendicular to the plane of the buckled silicene/germanene. Employing the random-phase approximation we analyze the magnetoplasmon spectrum. The dispersion relation has the same form as in a two-dimensional electron gas with the cyclotron and plasma frequencies modified due to the SOC and the field E_z . In the absence of SOC and E_z , our results agree well with recent experiments on graphene. The predicted effects could be tested by experiments similar to those on graphene and would be useful for future spintronics and optoelectronic devices.

Keywords: magnetoplasmons, correlation function in RPA, silicene or germanene, spin-orbit coupling, perpendicular electric field

(Some figures may appear in colour only in the online journal)

1. Introduction

Since its realization as a truly two-dimensional (2D) material, graphene has attracted much interest, both due to fundamental science and technological importance in various fields [1, 2]. However, the realization of a tunable band gap, suitable for device fabrications, is still challenging and SOC is very weak in graphene. To overcome these limitations researchers have been increasingly studying similar materials. One such material, called silicene, is a monolayer honeycomb structure of silicon and has been predicted to be stable [3]. Already several attempts have been made to synthesize it [4]. A similar material is germanene.

Despite controversy over whether silicene has been experimentally created or not [5], it is expected to be an excellent candidate materials because it has a strong SOC and an electrically tunable band gap [6–8]. It's a single layer of silicon atoms with a honeycomb lattice structure and compatible with silicon-based electronics that dominates the semiconductor industry. Silicene has Dirac cones similar to those of graphene and density functional calculations showed that the SOC gap induced in it is about 1.55 meV [6, 7]. Moreover, very recent theoretical studies predict the stability of silicene on non metallic surfaces such as graphene [9], boron nitride or SiC [10], and in graphene-silicene-graphene

structures [11]. Besides the strong SOC, another salient feature of silicene is its buckled structure with the A and B sublattice planes separated by a vertical distance 2ℓ so that inversion symmetry can be broken by an external electric field resulting in a staggered potential [8]. Accordingly, the energy gap in it and in germanene can be controlled electrically. Due to this unusual band structure, silicene and germanene are expected to show exotic properties such as quantum spin- and valley-Hall effects [8, 12, 13], magneto-optical and electrical transport [14, 15], etc.

Plasmons are quantized charge excitations due to the Coulomb interaction and a very important aspect in condensed matter physics not only from a fundamental point of view but also from a technological one [16–20]. In the presence of a magnetic field they are called magnetoplasmons and have been extensively studied theoretically [21–25] and observed experimentally [26–28] in graphene. The study of graphene (magneto)plasmons involves spatial confinement of light and enables them to operate at terahertz frequencies thus making it a promising material for optoelectronics. Next to graphene, which has a very weak SOC and no gap if not grown on a substrate, is silicene or germanene with strong SOC and a tunable band gap. So far plasmons in them have been studied only in the absence of a magnetic field [29–31].

The purpose of this work is to study magnetoplasmons in silicene or germanene. We evaluate the dynamical nonlocal dielectric response function to obtain the magnetoplasmon spectrum within the random-phase approximation (RPA). In particular, we take into account the effect of strong SOC and of an external electric field E_z applied perpendicular to its plane. Experiments can be done by incorporating the effects of SOC and E_z similar to the recent ones [26–28] on gapless graphene. In section 2 we present the basic formalism, in section 3 the density-density correlation function, and in section 4 the magnetoplasmons. Results and their discussion follow in section 5 and a summary in section 6.

2. Model formulation

We consider silicene or germanene in the (x, y) plane in the presence of intrinsic SOC and of an external electric field E_z applied along z axis in addition to a magnetic field $\mathbf{B} = B\hat{z}$. Electrons in silicene obey the 2D Dirac-like Hamiltonian [7, 8]

$$H^{\eta,s} = v_F(\eta\sigma_x\Pi_x + \sigma_y\Pi_y) + \eta s\lambda\sigma_z + V\sigma_z. \quad (1)$$

Here $\eta = 1(-1)$ represents the K (K') valley, $V = 2lE_z$ is the potential due to the uniform electric field E_z , $2l = 0.046$ nm is the distance between the two sublattice planes, and $\lambda = 4$ meV the SOC. For germanene we have $2l = 0.066$ nm and $\lambda = 43$ meV. Also, $\sigma_x, \sigma_y, \sigma_z$ are the Pauli matrices that describe the sublattice pseudospin, v_F the electron Fermi velocity, and $s = +1(-1)$ the up (down) electron spin. Further, $\Pi = \mathbf{p} - e\mathbf{A}$ is the canonical momentum and \mathbf{A} the vector potential that yields $\mathbf{B} = B\hat{z}$; we use the Landau gauge $\mathbf{A} = (0, Bx, 0)$. After diagonalizing the Hamiltonian we obtain the eigenvalues

$$E_n^{\eta,s} = \pm[\hbar^2\omega_c^2 n + V_\xi^2]^{1/2}, \quad E_0^{\eta,s} = -\eta V_\xi \quad (2)$$

where $V_\xi = V + \xi\lambda$ and $\xi = \eta s$. The corresponding eigenfunctions are

$$\Psi_n^{\eta,s} = \frac{e^{ik_y y}}{\sqrt{L_y}} \begin{pmatrix} -iC_n^{\eta,s} \phi_{n-1}(\bar{x}) \\ D_n^{\eta,s} \phi_n(\bar{x}) \end{pmatrix}, \quad \Psi_0^{\eta,s} = \frac{e^{ik_y y}}{\sqrt{L_y}} \begin{pmatrix} 0 \\ \phi_0(\bar{x}) \end{pmatrix}, \quad \Psi_0^{-,s} = \frac{e^{ik_y y}}{\sqrt{L_y}} \begin{pmatrix} \phi_0(\bar{x}) \\ 0 \end{pmatrix}. \quad (3)$$

Here $\omega_c = v_F\sqrt{2eB/\hbar}$, $\bar{x} = x - x_0$, $x_0 = l^2 k_y$, $l = \sqrt{\hbar/eB}$ is the magnetic length, and L_y the length of the silicene or germanene monolayer along the y direction. Moreover, $\phi_n(x) = e^{-x^2/2} H_n(x)/\sqrt{2^n n! \sqrt{\pi} l}$ and $H_n(x)$ are the Hermite polynomials. $C_n^{\eta,s}$ and $D_n^{\eta,s}$ are the normalization constants

$$C_n^{\eta,s} = [(1 \pm V_\xi/E_n^{\eta,s})/2]^{1/2}, \quad D_n^{\eta,s} = [(1 \mp V_\xi/E_n^{\eta,s})/2]^{1/2}. \quad (4)$$

The energy spectrum given in equation (2) is degenerate with respect to the wave vector k_y . The eigenfunctions for the K' valley can be obtained from equation (3), by interchanging ϕ_n and ϕ_{n-1} , and the corresponding eigenvalues from equation (2) with $\eta = -1$.

3. Density–density correlation function

3.1. Finite frequencies

The dynamic and static response properties of an electron system are embodied in the structure of the density–density correlation function which we evaluate in the RPA. The RPA treatment presented here is by its nature a high-density approximation that has been successfully employed in the study of collective excitations in 2D graphene-like systems both with and without an applied magnetic field [16–24]. It has been found that the RPA predictions of plasmon spectra are in excellent agreement with experimental results [26–28]. Following this technique, one can express the dielectric function as

$$\epsilon(q, \omega) = 1 - v_c(q)\Pi_0(q, \omega), \quad (5)$$

where $v_c(q) = 2\pi e^2/\kappa q$ is the 2D Fourier transform of the Coulomb potential with wave vector q and κ the effective background dielectric constant. The non-interacting density–density correlation function is obtained as

$$\Pi_0(q, \omega) = \frac{1}{A} \sum_{n,n',k_y,k_y'} [f(E_n^{\eta,s}) - f(E_{n'}^{\eta,s})] |\langle \alpha' | e^{-iq\cdot\mathbf{r}} | \alpha \rangle|^2 \times [E_n^{\eta,s} - E_{n'}^{\eta,s} + \hbar\omega + i\gamma]^{-1}, \quad (6)$$

where A is the area of the system and $|\alpha\rangle = |n, \eta, s, k_y\rangle$. Here γ is the the width of the energy levels due to scattering and is an infinitesimally small quantity in samples with high mobility [28]. The matrix element in equation (6) is evaluated in the appendix; the result is

$$|\langle \alpha' | e^{-iq\cdot\mathbf{r}} | \alpha \rangle|^2 = J_{n,n'}(u) = \delta_{k_y', k_y - q_y} \times \left\{ [C_n^{\eta,s} C_{n'}^{\eta,s}] F_{n-1, n'-1}(u) + [D_n^{\eta,s} D_{n'}^{\eta,s}] F_{n,n'}(u) \right\}^2, \quad (7)$$

where $u = l^2 q^2/2$. For $n \leq n'$ we have $[F_{n,n'}(u)]^2 = (n!/n'!) e^{-u} u^{n'-n} [L_n^{n'-n}(u)]^2$ and for $n' \leq n$ the same expression with n and n' interchanged. The sum over k_y in equation (6) can be evaluated using the prescription ($k_0 = L_x/2l^2$)

$$\sum_{k_y} \rightarrow \frac{L_x}{2\pi} g_s g_v \int_{-k_0}^{k_0} dk_y = \frac{A}{D_0} g_s g_v, \quad (8)$$

where $D_0 = 2\pi l^2$, g_s and g_v are the spin and valley degeneracies, respectively. We use $g_s = g_v = 1$ in the present work due to the lifting of the spin and valley degeneracies in silicene or germanene.

We now use the transformation $k_y \rightarrow -k_y$ and the fact that $E_n^{\eta,s}(k_y)$ is an even function of k_y , see equation (2). Then if we interchange n and n' and perform the k_y integration using equations (7) and (8), we can write the non-interacting density–density correlation function as

$$\Pi_0(q, \omega) = \frac{1}{D_0} \sum_{n,n'} J_{nn'}(u) f(E_n^{\eta,s}) \left[(E_n^{\eta,s} - E_{n'}^{\eta,s} + \hbar\omega + i\gamma)^{-1} - (E_{n'}^{\eta,s} - E_n^{\eta,s} + \hbar\omega + i\gamma)^{-1} \right]. \quad (9)$$

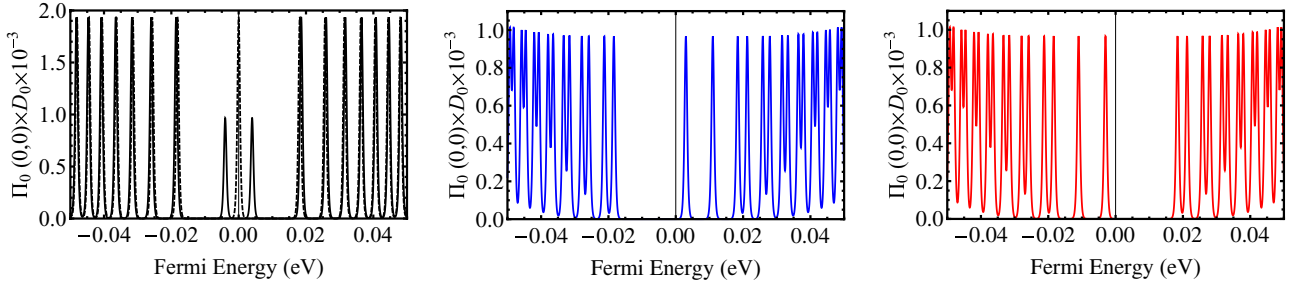


Figure 1. Static density–density correlation function in the long-wavelength limit $q \rightarrow 0$ versus Fermi energy E_F . We vary the field E_z and the SOC strength λ . Left panel: the dashed and solid curves are for $V = \lambda = 0$ and $V = 0$ meV and $\lambda = 4$ meV. The other two panels are for $V = 7$ meV and $\lambda = 4$ meV; the middle panel is for the K valley and the right one for the K' valley. The degeneracy of the LLs is lifted.

The real and imaginary parts of $\Pi_0(q, \omega)$ can be obtained from the identity $1/(x \pm i\gamma) = (\wp/x) \mp i\pi\delta(x)$ where \wp denotes the principal value of $1/x$. The real part of equation (9) reads

$$\Pi_1(q, \omega) = \frac{1}{D_0} \sum_{n,n'} J_{nn'}(u) [I_1(\omega) + I_1(-\omega)], \quad (10)$$

with

$$I_1(\omega) = f(E_n^{\eta,s}) / [E_n^{\eta,s} - E_{n'}^{\eta,s} + \hbar\omega], \quad (11)$$

while the imaginary part is written as

$$\Pi_2(q, \omega) = \frac{\pi}{D_0} \sum_{n,n'} J_{nn'}(u) [I_2(\omega) - I_2(-\omega)], \quad (12)$$

with

$$I_2(\omega) = f(E_n^{\eta,s}) \delta(\hbar\omega + E_{n'}^{\eta,s} - E_n^{\eta,s}). \quad (13)$$

Equations (10)–(13) will be the starting point of our treatment of magnetoplasmons. Their form makes clear their even and odd symmetry with respect to ω . These functions are the essential ingredients for theoretical considerations of such diverse problems as high-frequency and steady-state transport, static and dynamic screening, and correlation phenomena.

3.2. Limit $\omega = q = 0$

The non-interacting density–density correlation function is obtained from equation (6) in the static and long wavelength limit, $\omega = q = 0$. Thus equation (6) becomes

$$\Pi_0(0, 0) = \frac{1}{D_0} \sum_{n,n',\pm} \frac{f(E_n^{\eta,s}) - f(E_{n'}^{\eta,s})}{E_n^{\eta,s} - E_{n'}^{\eta,s}}, \quad (14)$$

where the summation over $+/-$ represents electrons/holes. With the zero-temperature limit, this turns into a series of delta functions, $\delta(E_F \pm E_n^{\eta,s})$ [32, 33]. Making the replacement $\delta(E) = (\Gamma/\pi)/(\mathbb{E}^2 + \Gamma^2)$, we arrive at

$$\Pi_0(0, 0) = \frac{1}{2\pi D_0} \sum_{n=0,\pm}^{\infty} \frac{(2 - \delta_{0,n})\Gamma}{(E_F - E_n^{\eta,s})^2 + \Gamma^2}, \quad (15)$$

where Γ is the level width. Then the density–density correlation function is proportional to the density of states at

the Fermi energy, $\Pi_0(0, 0) = D(E_F)$. At finite temperatures though it is given by [32, 33]

$$\Pi_0(0, 0) = \int_{-\infty}^{+\infty} [-\partial f(E)/\partial E] D(E) dE. \quad (16)$$

The density–density correlation function shows the lifting of the four-fold degeneracy at $E_F = 0$ (Dirac point) at zero temperature. At $T = 0$ and $E_F = 0$ this function vanishes in the limit of zero SOC and E_z , simply because it becomes the same as that of graphene at the Dirac point ($E_F = 0$) with a completely filled valence band and completely empty conduction band. The corresponding carrier density vanishes and implies that no intrinsic graphene plasmons are possible (more generally, Dirac plasmons). This means that the screening is absent to linear order except for the renormalization of the dielectric constant term. However, when the Fermi level is away from $E_F = 0$ or at nonzero temperature, the density–density correlation function shows doubly degenerate spin and valley splitting of the Landau levels (LLs) and the linear screening is expected to become appropriate. Moreover, these results can be reduced to those for gapless graphene derived and discussed in [33] (see figure 1) in the limit of zero SOC and E_z .

We show numerical results of equation (16) as a function of the Fermi energy in figure 1. We find that the $n = 0$ LL is split into four levels and all other LLs ($n > 0$) into two. The valley degeneracy is lifted by the application of the field E_z and the spin degeneracy by the SOC. This is consistent with the eigenvalues given by equation (2). We use $B = 1$ Tesla, $T = 3$ K, and vary the field energy $V = 2lE_z$ and the SOC strength. The left panel is drawn for $V = \lambda = 0$ (dashed curves) and $V = 0$ meV and $\lambda = 4$ meV (solid curves). The other two panels are for $V = 7$ meV and $\lambda = 4$ meV; the middle panel is for the K valley and the right one for the K' valley.

In figure 1 the SOC and field split the LLs in two groups: in accordance with equation (2), $\eta, s = \pm$, we label them as $+\equiv +, +\equiv -, -$ and $-\equiv -, +\equiv +, -$. Every $n \neq 0$ LL is doubly degenerate in each group and consists of a spin-up state from one valley and a spin-down state from the other valley. The LL splitting between the two groups is symmetric in the valence and conduction band due to the symmetry in equation (2). The four-fold spin and valley degeneracy of the $n = 0$ LL is lifted by the SOC and electric field energy.

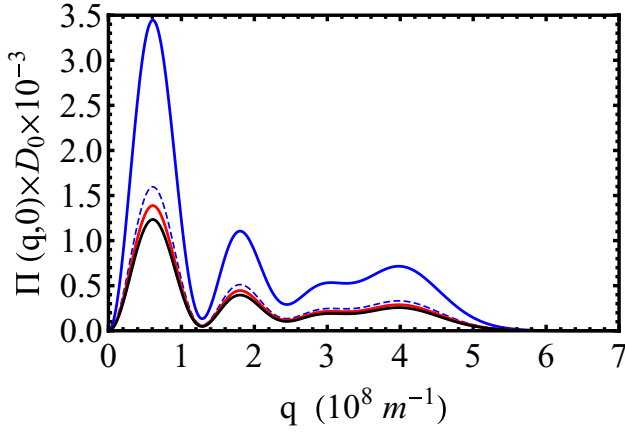


Figure 2. Static density–density correlation function versus the wave vector q . We vary the electric field energy V and the SOC strength λ . Black curves: $V = \lambda = 0$; red curves $V = 0$ meV, $\lambda = 4$ meV; blue curves $V = 10$ meV and $\lambda = 4$ meV. The solid and dashed curves pertain, respectively, to spin up and spin down in the K valley or spin down and spin up in the K' valley. Here we cannot distinguish between the black (or red) solid and dashed curves as there is no spin or valley splitting for the chosen parameters.

3.3. Zero frequency

The static limit $\omega \rightarrow 0$ of equation (6) is obtained with the help of equations (7) and (8). In this limit $\text{Im}\Pi_0(q, \omega) \rightarrow 0$ and equation (6) gives

$$\Pi_0(q, 0) = \frac{1}{D_0} \sum_{n,n'} \frac{f(E_n^{\eta,s}) - f(E_{n'}^{\eta,s})}{E_n^{\eta,s} - E_{n'}^{\eta,s}} J_{nn'}(u). \quad (17)$$

We show numerical results for $\Pi_0(q, 0)$ as a function of the wave vector q in figure 2. We use the parameters $B = 5$ Tesla, $T = 10$ K, and vary the field energy $V = 2lE_z$ and the SOC strength λ . The black curves are for $V = \lambda = 0$, the red ones for $V = 0$ meV and $\lambda = 4$ meV, and the blue curves for $V = 10$ meV and $\lambda = 4$ meV. The solid and dashed curves pertain, respectively, to spin up and K valley and to spin down and K' valley.

In the usual 2DEG the screening wave vector is independent of the carrier density but for graphene or silicene it is proportional to the square root of the density [16]. First, in the limit of zero magnetic field B the static correlation function remains constant and equal to the electronic density of states up to the wave vector of $q = 2k_F$; there are two contributions to it that stem from intraband and interband plasmons, respectively. In the large momentum transfer regime of figure 2, $q \sim 5$ (10^8 m^{-1}), the static screening for the intraband case decreases linearly with q , which is consistent with the case of gapless graphene in the limit of zero (see figure 2 of [16] and figure 4 of [32]) and finite [23] magnetic field. There is no possibility of zero-energy plasmon excitations in the *intraband* region (valence or conduction band).

We find a similar behaviour for finite B except in the small wave vector limit. In contrast with its behaviour at $B = 0$, the static correlation function tends to zero as $\Pi_0(q \rightarrow 0, 0) \propto q^2$ for finite B [23]. This is due to the fact that the main contribution to it comes from the $q = 0$ excitations in the

vicinity of E_F . Whereas at $B = 0$ there are $q \rightarrow 0$ excitations whose energy tends to zero, E_F now lies in a cyclotron gap between the highest occupied Landau level n_F and lowest unoccupied $n_F + 1$. This gap must be overcome by small- q excitations, such that its spectral weight approaches zero. The static correlation function also coincides with the density of states at E_F because the latter vanishes for finite fields B when E_F is in the gap. Further, the oscillatory behaviour of the static correlation function below $2k_F$ is due to *intraband* transitions, whether E_F is in the valence or conduction band ($n_F + 1, n_F$).

4. Magnetoplasmons

Magnetoplasmons are readily furnished by the singularities of the function $\Pi_1(q, \omega)$, from the roots of the longitudinal magnetoplasmon dispersion relation obtained from equation (9) as

$$1 - v_c(q)\Pi_1(q, \omega) = 0, \quad (18)$$

along with the condition $\Pi_2(q, \omega) = 0$ to ensure long-lived excitations [22, 23, 29, 30], which is in excellent agreement with high-mobility graphene samples [28].

For weak damping the decay rate γ , determined by equations (10) and (12), is given by equation 22 of [30]. Since we are primarily interested in the long-wavelength behavior of undamped magnetoplasmons, described by $\gamma \propto \Pi_2(q, \omega) = 0$, we treat them by solving equation (18). With the help of equation (10) we find its roots are obtained by solving

$$1 = \frac{e^2}{kql^2} \sum_{n,n'} J_{nn'}(u) [I_1(\omega) + I_1(-\omega)]. \quad (19)$$

Using equation (11) we can write

$$I_1(\omega) + I_1(-\omega) = \frac{2\Delta_{n,n'}^{\eta,s}}{\hbar^2\omega^2 - (\Delta_{n,n'}^{\eta,s})^2} f(E_n^{\eta,s}), \quad (20)$$

where $\Delta_{n,n'}^{\eta,s} = E_{n'}^{\eta,s} - E_n^{\eta,s}$. Next we expand $J_{nn'}(u)$ to lowest order in its argument (low wave-number expansion). This amounts to considering only the $n' = n \pm 1$ terms in equation (19). The inter-Landau level plasmon modes under consideration arise from neighbouring Landau levels, that is, from $n' = n \pm 1$. Then using the expansion [34]

$$L_n^l(u) = \sum_{m=0}^n \frac{(-1)^m (n+1)!}{(l+m)!(n-m)! m!} u^m \quad \text{for } l > 0 \text{ and retaining only terms}$$

that are constant or linear in u we get

$$J_{n,n+1}(u) \rightarrow nuG^C + (n+1)uG^D, \quad (21)$$

$$J_{n,n-1}(u) \rightarrow (n-1)uG^C + nuG^D. \quad (22)$$

Here $G^C = (1 + r_\xi)/2$, $G^D = (1 - r_\xi)/2$, and $r_\xi = V_\xi / [\hbar^2\omega_c^2 n + V_\xi^2]^{1/2}$. The factors G^C and G^D arise from the normalization of the eigenstates and in the limit $\lambda = E_z = 0$ are both equal to $1/2$.

To obtain the magnetoplasmon spectrum, we evaluate $\Delta_{n,n'}^{\eta,s}$ for $n' = n \pm 1$. We find

$$\Delta_{n,n\pm 1}^{\eta,s} = \pm \hbar\omega_c / (2[n + (V_\xi/\hbar\omega_c)^2]^{1/2}). \quad (23)$$

Substitution of equations (20)–(22) into equation (19) yields

$$1 = \frac{e^2 q}{\kappa} \sum_n \frac{|\Delta_{n,n\pm 1}^{\eta,s}|}{\hbar^2 \omega^2 - (\Delta_{n,n\pm 1}^{\eta,s})^2} f(E_n^{\eta,s}). \quad (24)$$

For inter-LL excitations near the Fermi energy E_F we can approximate n by n_F in $\Delta_{n,n\pm 1}^{\eta,s}$, where n_F is the LL index corresponding to E_F . This gives

$$\begin{aligned} \hbar^2 \omega^2 &= (\hbar^2 \omega_c^2 / (4[n_F + (V_\xi / \hbar \omega_c)^2])) \\ &\times \left[1 + \frac{2e^2 q [n_F + (V_\xi / \hbar \omega_c)^2]^{1/2}}{\kappa \hbar \omega_c} \sum_n f(E_n^{\eta,s}) \right]. \end{aligned} \quad (25)$$

With E_F in the conduction band ($E_F^2 = \hbar^2 \omega_c^2 n_F + V_\xi^2$) equation (25) can be expressed as

$$\omega^2 = \tilde{\omega}_c^2 + \tilde{\omega}_p^2, \quad (26)$$

where

$$\tilde{\omega}_c = \omega_c [\hbar \omega_c / (2(\hbar^2 \omega_c^2 n_F + V_\xi^2)^{1/2})], \quad (27)$$

and

$$\tilde{\omega}_p = \omega_p [v_F / (\hbar^2 \omega_c^2 n_F + V_\xi^2)^{1/4}], \quad (28)$$

with $\omega_p = [e^2 q \pi n_c / \kappa]^{1/2}$ and $n_c = \sum_n f(E_n^{\eta,s}) / (\pi \ell^2)$ the 2D carrier density.

It is interesting that equation (24) can be applied to the usual 2DEG for which $\Delta_{n,n\pm 1}^{\eta,s} = \pm \hbar \omega_c$. Then we obtain again equation (26) with $\tilde{\omega}_c$ and $\tilde{\omega}_p$ replaced, respectively, by $\omega_c = eB/m$ and $\omega_p = [e^2 q \pi n_c / \kappa]^{1/2}$, that is, the well-known plasmon dispersion relation. One can also take the limit $V_\xi \rightarrow 0$ in equations (24)–(28) and obtain the dispersion relation for monolayer graphene [23, 28]. Then $\Delta_{n,n\pm 1}^{\eta,s} = \pm \hbar \omega_c / (2n^{1/2})$, $\tilde{\omega}_c = \omega_c / (2\sqrt{n_F})$, and $\tilde{\omega}_p = (v_F / (2n_F^{1/4} \sqrt{\hbar \omega_c})) \omega_p$.

In the limit of zero magnetic field, equations (26)–(28) reduce to recent work on silicene and germanene [29, 30]. Moreover, in the limit of zero SOC and E_z , these relations are the same as that for high-mobility graphene samples [28] and could be applied to highly doped graphene samples [26, 27] (for very large n_F in equation (25)). The q dependence of equation (26), namely the \sqrt{q} behaviour, is common to 2D electron gas systems while the carrier density dependence is characteristic of the linear-in- k dispersion relation of massless Dirac fermions, for which $E_F = \hbar v \sqrt{\pi n_c}$. However, in the present case we can see the effects of gapped silicene or germanene with massive Dirac fermions and spin/valley splitting due to the combination of the SOC and the electric field E_z .

5. Discussion of results

A closer analytical examination of equation (26) shows the following aspects of the gapped magnetoplasmon spectrum. If we set $E_z = 0$ in equation (26) we obtain a SOC-induced, small-gap magnetoplasmon spectrum. Increasing E_z , we obtain a larger gap, splitting and tuning of plasmons in silicene by combining it with the SOC. If we use a field E_z

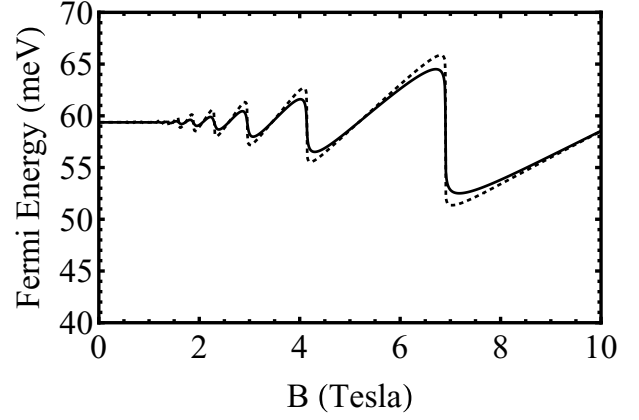


Figure 3. Fermi energy as a function of magnetic field for fixed values $V = 10$ meV, $\lambda = 4$ meV, and $n_c = 0.5 \times 10^{16} \text{ m}^{-2}$. The temperature is varied such that $T = 10$ K (solid) and $T = 5$ K (dotted).

comparable to the SOC strength λ , then we expect splitting of the magnetoplasmon modes due to the combination of the two in the quantity $V + \eta s \lambda$. With further increase in E_z , e.g. $E_z = 2\lambda$ we can see an enhanced spin and valley splitting of the magnetoplasmon spectrum due to the $V + \eta s \lambda$ factor in equation (21). Moreover, we note that the realization of topological phase transitions could also be observed in the magnetoplasmon spectrum if we take E_z zero or less than λ (spin-Hall regime), comparable to λ (semi-metallic regime), and then twice λ (valley-Hall regime). The spin-Hall regime is a topological insulator while the valley-Hall one is a band insulator. For $B \rightarrow 0$ these transitions are consistent with recent plasmon predictions [29, 30]. Below we consider the effect of an external field B using the parameters [7, 26–30]: $q = \pi / 100 \text{ nm}^{-1}$, $v_F = 0.5 \times 10^6 \text{ m s}^{-1}$, $\lambda = 4$ meV for silicene (43 meV for germanene) on SiC with dielectric constant $\kappa \simeq 4$ (different values do not qualitatively affect the results), and carrier density $n_c = 0.5 \times 10^{16} \text{ m}^{-2}$ giving $E_F = 41.3$ meV.

The changes in the density of states $D(E)$ discussed in section 3 and the approximations used to obtain the magnetoplasmons are reflected in the dependence of E_F , e.g. on the magnetic field. At finite temperatures the 2D carrier density n_c is $n_c = \int_{-\infty}^{\infty} D(E) f(E) dE$, with $D(E)$ for the LL spectrum obtained as

$$D(E) = \frac{1}{D_0} \left(\frac{1}{2} \sum_{\eta,s} \delta(E - E_0^{\eta,s}) + \sum_{n=1,\eta,s} \delta(E - E_n^{\eta,s}) \right); \quad (29)$$

the factor 1/2 refers the fact the degeneracy of the zero LL is half that of the other LLs. Using equation (29) the result for n_c becomes

$$n_c = \frac{1}{D_0} \left(\frac{1}{2} \sum_{\eta,s} f(E_0^{\eta,s}) + \sum_{n=1,\eta,s} f(E_n^{\eta,s}) \right). \quad (30)$$

For fixed carrier density, this determines E_F implicitly by solving numerically equation (30). We show the resulting E_F , as a function of the magnetic field B in figure 3, for

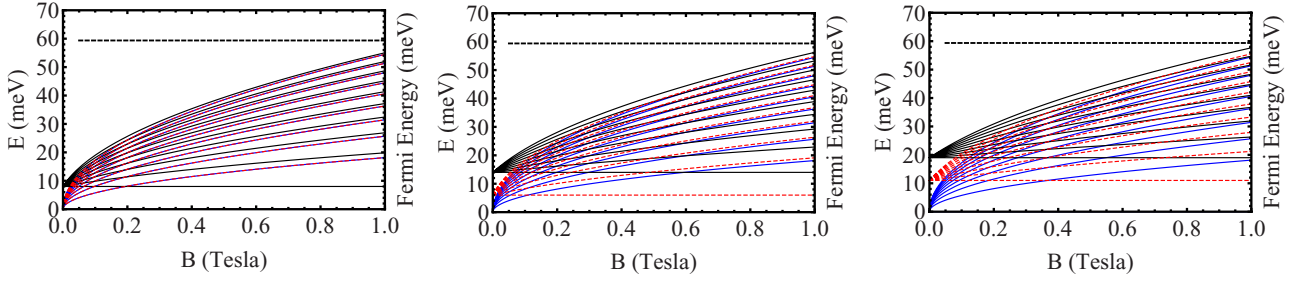


Figure 4. Band structure of silicene as a function of the magnetic field B . The blue curves correspond to $\lambda = V = 0$ and the black and red dotted ones to E_n^+ and E_n^- , respectively. The black dotted line shows E_F versus B evaluated numerically using equation (30). In the left panel we cannot distinguish between the blue and red dotted curves because at $\lambda = V = 4$ meV the gap is zero for the $(V - \lambda)$ curves. In the middle panel we see a clear degree of spin and valley splitting for $\lambda = 4$ meV and $V = 10$ meV. The right panel, for $\lambda = 4$ meV and $V = 15$ meV, shows a significant degree of spin and valley splitting by electrical tuning.

$V = 10$ meV, $\lambda = 4$ meV, $T = 10$ K, and $n_c = 0.5 \times 10^{16} \text{ m}^{-2}$. E_F remains constant for low B below 2T, that is, in the limit of large n ; above this value we see the jumps as E_F crosses the LLs.

We present the eigenvalues given by equation (2) as a function of the field B for fixed values of λ and E_z in figure 4. We also include the E_F versus field B curve (dotted line) for comparison and further discussion. We find the following: (i) In the limit of $\lambda = \ell E_z = 0$ (blue curves), we obtain the \sqrt{B} dependence of the LL energies. In contrast, for finite λ and variable E_z (black and red dotted curves), the energies of the lower LLs grow linearly with B rather than with \sqrt{B} because of the massive Dirac fermions in silicene or germanene. (ii) The combination of the field energy $V = 2\ell E_z$ and λ splits the LLs in two groups designated as E_n^\pm , with $E_n^+ \equiv E_n^{+,+} = E_n^{-,-}$ and $E_n^- \equiv E_n^{-,+} = E_n^{+,-}$. (iii) The energies of the two groups of LLs in the valence or conduction band have not only different slopes versus B but also shift rigidly for $B \rightarrow 0$ due to the finite band gap either by λ or by the field E_z . However, every $n \neq 0$ LL is still doubly degenerate in each group, consisting of a spin-up state from one valley and a spin-down state from the other valley. A crossing occurs between the two groups, which is symmetric in the valence and conduction band due to the symmetry in equation (2).

In figure 5 we show the magnetoplasmon spectrum as a function of the field B for fixed $E_F = 41.3$ meV. For comparison with graphene experiments [28], we show numerical results using equation (26) for $\lambda = V = 0$ (blue curve). These results agree well with equation (1) and figure 2 of [28], exhibiting dependence on \sqrt{B} , if we replace $v_F = 0.5 \times 10^6 \text{ m s}^{-1}$ by its value in graphene $v_F = 1 \times 10^6 \text{ m s}^{-1}$. In the middle panel, for finite λ and $V = 2\ell E_z$, we found two curves, the red dotted ($V - \lambda$) and black ($V + \lambda$) showing a spin and valley splitting. The red dotted curve is the same as the blue one and we can't distinguish between the two because the gap for the red dotted line vanishes due to $\lambda - 2\ell E_z = 0$. As the gap due to λ and V is small and we are in a highly doped regime, we can see a split between the red dotted and black curve for two magnetoplasmon modes $\hbar\omega_\pm$ defined as $\hbar\omega_+ = \hbar\omega_{+,+} = \hbar\omega_{-,-}$ and $\hbar\omega_- = \hbar\omega_{-,+} = \hbar\omega_{+,-}$. Increasing $V = 2\ell E_z = 10$ meV, we see an enhanced splitting between red dotted and black curves for fixed $\lambda = 4$ meV (middle panel). Here the blue and red dotted curves are weakly

separated as the gap vanishes for the blue and red dotted curves $V - \lambda = 6$ meV. With further increase in V , $V = 15$ meV, we obtain a further enhanced splitting between the black and red dotted curves of the magnetoplasmon modes as shown in the right panel for fixed $\lambda = 4$ meV. We also note that the blue and red dotted lines are well separated as gap is zero for the blue and $V - \lambda = 11$ meV for the red dotted curve.

We contrast our results with those of recent graphene experiments on high-mobility or weakly doped samples [28], in the limit $\lambda = 2\ell E_z = 0$, by further decreasing the Fermi energy close to the Dirac point. First, we show the magnetoplasmon spectrum as a function of the field B for $E_F = 26$ meV in figure 6. We found a clear splitting between the black and red dotted curves for $\lambda = 2\ell E_z = 4$ meV (left panel) as in the left panel of figure 5. As λ and E_z are small and we are in a weakly doped regime, we can see a strong splitting for the magnetoplasmon modes $\hbar\omega_\pm$. Again here we cannot distinguish between the red dotted and blue curves for the same reason as in figure 5. Upon increasing V , e.g. to $V = 10$ meV, we see a large splitting between the red dotted and black curves for fixed $\lambda = 4$ meV (middle panel). We can weakly distinguish between the blue and red dotted curves here since the gap is $V - \lambda = 6$ meV for the red dotted curve and zero for the blue one. With further increase in V , $V = 15$ meV, we obtain a significant splitting between the red dotted and black curves of the magnetoplasmon modes as shown in the right panel. Here we also note that the blue and red dotted curves are well separated compared to those in the right panel of the figure 5. Again the results exhibit a square-root dependence on B and agree with recent graphene theory [21–25] and experiments [28] in the limit $\lambda = 2\ell E_z = 0$ provided we use $v_F = 1 \times 10^6 \text{ m s}^{-1}$.

The experimentally observed [28], \sqrt{B} dependence of the spectrum referred to above, in the limit $\lambda = V \rightarrow 0$, applies to high-mobility *weakly-doped* graphene samples, see figure 6. For *highly-doped* samples [26, 27] though that involve values of $E_F \gg \lambda, V$, with E_F of the order of 200–300 meV, the magnetoplasmon gaps and splittings reported above will be very difficult to achieve as they would require unrealistically high values of V . Notice though that our analysis for silicene also holds for germanene, a monolayer of germanium, which has a much stronger SOC than silicene [7, 8], $\lambda \approx 43$ meV. In both cases the predicted gaps and splittings are sizeable for E_F not too far from the Dirac point.

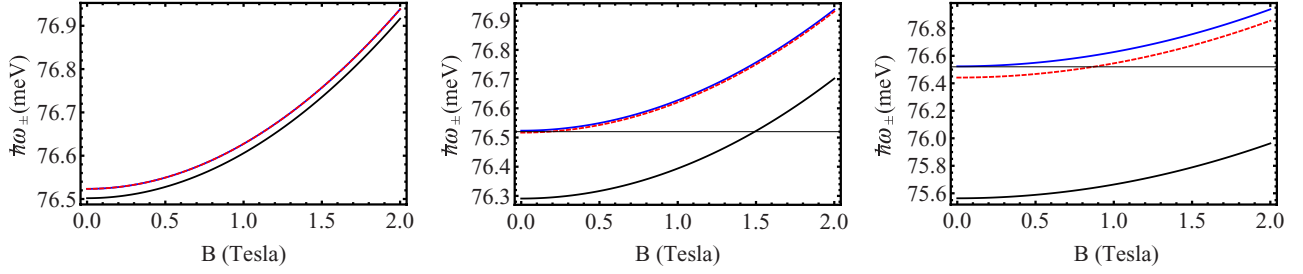


Figure 5. Magnetoplasmons as a function of the magnetic field B for a fixed $E_F = 41.3$ meV. Blue curves correspond to $\lambda = V = 0$. Black and red dotted curves represent $\hbar\omega_+$ and $\hbar\omega_-$, respectively. In the left panel, with $\lambda = V = 4$ meV, we cannot distinguish between the red and blue dotted curves because at equal amount of V and λ energies, the gap is zero for the $(V - \lambda)$ curves. The middle panel, for $\lambda = 4$ meV and $V = 10$ meV, shows a clear signature of spin and valley splitting. The right panel, for $\lambda = 4$ meV and $V = 15$ meV, shows a significant spin and valley splitting by electrical tuning. The colour code is the same as in figure 4.

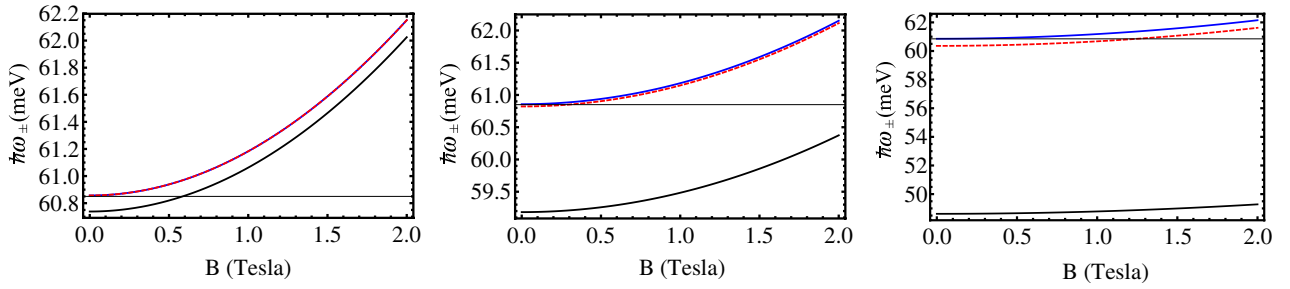


Figure 6. Magnetoplasmons as a function of the magnetic field B for a fixed $E_F = 26$ meV. The parameters and curve marking are the same as in figure 5.

Another feature of our results is the magnetoplasmon gaps. Although not yet experimentally confirmed, the SOC induced gap in silicene is about 1.55 meV [6, 7] and is expected to be observed using existing experimental techniques. In the present work on electrically tunable magnetoplasmons in silicene, we have obtained a gap of about 1 meV in figure 5 and 12 meV in figure 6 tuned by an external perpendicular electric field, which can be further enhanced by increasing this electric field and lowering the Fermi energy of the system close to the Dirac point. We believe that this gap can be observed in experiments similar to those on high-mobility graphene samples studying magnetoplasmons [28].

A possible extension of our work would be to include an in-plane electric field and study magneto-electric-plasmons. One could then use the eigenfunctions and eigenvalues derived in [36] for $E_z = \lambda = 0$ as a starting point.

6. Summary

We showed electrically tunable effects in the magnetoplasmon spectrum of silicene and germanene due to the spin and valley polarization. Employing the RPA and including the effects of SOC and of an external electric field, we found a significant splitting of the magnetoplasmon spectrum. Our results agree well with graphene theory and experiments in the limit of vanishing SOC and electric field provided E_F is not too far from the Dirac point, that is, for *weakly-doped* graphene samples [28], if we use graphene's value for v_F . We expect that experimental studies of these novel phenomena in silicene, similar to those of [28], will be very appropriate since they directly bear on the many-body properties of silicene or

germanene. Encouraging in this direction is the very recently reported local formation of high-buckled silicene nanosheets realized on a MoS₂ surface [35].

Appendix A.

Below we outline the derivation of equation (8). The factor $J_{\alpha,\alpha'}$ in equation (7) is given by

$$J_{\alpha,\alpha'} = \langle \alpha' | |e^{-i\mathbf{q}\cdot\mathbf{r}}| | \alpha \rangle^2 = \langle \alpha' | |e^{-i\mathbf{q}\cdot\mathbf{r}}| | \alpha \rangle \times \langle \alpha | |e^{i\mathbf{q}\cdot\mathbf{r}}| | \alpha' \rangle, \quad (\text{A.1})$$

where $|\alpha\rangle = |s, n, \eta, k_y\rangle$. Using the eigenfunctions given by equation (3), equation (A.1) takes the form

$$\langle \alpha' | |e^{-i\mathbf{q}\cdot\mathbf{r}}| | \alpha \rangle = \frac{1}{L_y} \sum_{n,\eta,s} \int dy e^{i(k_y - k'_y - q_y)y} \times \int_{-\infty}^{\infty} dx \begin{pmatrix} -iC_n^{\eta,s} \phi_{n-1}(\bar{x}) \\ D_n^{\eta,s} \phi_n(\bar{x}) \end{pmatrix}^T e^{-iq_x x} \begin{pmatrix} -iC_n^{\eta,s} \phi_{n-1}(\bar{x}) \\ D_n^{\eta,s} \phi_n(\bar{x}) \end{pmatrix}, \quad (\text{A.2})$$

where the superscript T denotes the transpose of the column vector. With the help of the identity $(1/L_y) \int dy e^{i(k_y - k'_y - q_y)y} = \delta_{k'_y, k_y - q_y}$ we can write equation (A.2) as

$$\langle \alpha' | |e^{-i\mathbf{q}\cdot\mathbf{r}}| | \alpha \rangle = \delta_{k'_y, k_y - q_y} \sum_{n,\eta,s} \left[F_{n',n}(-q_x, k_y - q_y, k_y) + F_{n'-1,n-1}(-q_x, k_y - q_y, k_y) \right]. \quad (\text{A.3})$$

Similarly,

$$\langle \alpha | |e^{i\mathbf{q}\cdot\mathbf{r}}| | \alpha' \rangle = \delta_{k'_y, k_y - q_y} \sum_{n,\eta,s} \left[F_{n,n'}(q_x, k_y, k_y - q_y) + F_{n-1,n'-1}(q_x, k_y, k_y - q_y) \right]. \quad (\text{A.4})$$

Combining equations (A.3) and (A.4), we arrive at

$$J_{n,n'}(u) = \delta_{k'_y, k_y - q_y} \sum_{n, \eta, s} \left[F_{n',n}(-q_x, k_y - q_y, k_y) \times F_{n,n'}(q_x, k_y, k_y - q_y) + F_{n'-1, n-1}(-q_x, k_y - q_y, k_y) \times F_{n-1, n'-1}(q_x, k_y, k_y - q_y) \right]. \quad (\text{A.5})$$

Now we proceed with the evaluation of $F_{n'n}(-q_x, k_y - q_y, k_y)$. Using the explicit form of the harmonic oscillator functions $\phi_n(\bar{x})$ we have

$$F_{n'n}(-q_x, k_y - q_y, k_y) = \frac{[D_{n'}^{\eta,s} D_n^{\eta,s}]}{l^2 \sqrt{\pi} 2^n 2^{n'} n! n'!} \times \int_{-\infty}^{\infty} dX e^{-(X+l(k_y-q_y))^2/2} \times H_{n'}(X+l(k_y-q_y)) e^{-iq_x X} e^{-(X+l k_y)^2/2} H_n(X+l k_y), \quad (\text{A.6})$$

where $X = x/l$. Making the change $Y = X + l k_y + l(-q_y + i q_x)/2$ in equation (A.6) yields

$$F_{n'n}(-q_x, k_y - q_y, k_y) = \frac{[D_{n'}^{\eta,s} D_n^{\eta,s}]}{\sqrt{\pi} 2^n 2^{n'} n! n'!} e^{-u^2} e^{i l^2 q_x (-q_y + 2k_y)/2} \times \int_{-\infty}^{\infty} dY e^{-Y^2} H_{n'}(Y - l(q_y + i q_x)/2) \times H_n(Y - l(q_y - i q_x)/2), \quad (\text{A.7})$$

where $u = l^2 q^2/2$. The integral over Y is tabulated in [34], pp. 838 #7.377. The result for $n \leq n'$ is

$$F_{n'n}(-q_x, k_y - q_y, k_y) = (n!/n')^{1/2} e^{-u/2 + i l^2 q_x (-q_y + 2k_y)/2} \times \left[l(q_y - i q_x) / \sqrt{2} \right]^{n'-n} L_{n'-n}^{n'-n}(u). \quad (\text{A.8})$$

For $n' \leq n$, the result is given by equation (A.8) with n and n' interchanged. Using equations (A.5) and (A.8) we arrive at equation (7),

$$J_{n,n'}(u) = |\langle \alpha' | e^{-i q \cdot r} | \alpha \rangle|^2 = \delta_{k'_y, k_y - q_y} \left\{ [D_{n'}^{\eta,s} D_n^{\eta,s}] F_{nn'}(u) + [C_{n'}^{\eta,s} C_n^{\eta,s}] F_{n-1, n'-1}(u) \right\}^2, \quad (\text{A.9})$$

with $F_{nn'}(u)$ given after equation (7) in the text.

References

[1] Novoselov K S, Geim A K, Morozov S, Jiang D, Zhang Y, Dubonos S, Grigorieva I and Firsov A A 2004 *Science* **306** 666
 [2] Castro A H, Guinea F, Peres N M R, Novoselov K S and Geim A K 2009 *Rev. Mod. Phys.* **81** 109
 [3] Guzmán-Verri G G and Lew L C 2007 *Phys. Rev. B* **76** 075131
 Lebègue S and Eriksson O 2009 *Phys. Rev. B* **79** 115409
 [4] Vogt P, Padova P D, Quaresima C, Avila J, Frantzeskakis E, Asensio M C, Resta A, Ealet B and Lay G L 2012 *Phys. Rev. Lett.* **108** 155501

Fleurence A, Friedlein R, Ozaki T, Kawai H, Wang Y and Yamada-Takamura Y 2012 *Phys. Rev. Lett.* **108** 245501
 [5] Lin C L, Arafune R, Kawahara K, Kanno M, Tukahara N, Minamitani E, Kim Y, Kawai M and Takagi N 2013 *Phys. Rev. Lett.* **110** 076801
 Guo Z X, Furuya S, Iwata J and Oshiyama A 2013 *J. Phys. Soc. Japan* **82** 063714
 Wang Y P and Cheng H P 2013 *Phys. Rev. B* **87** 245430
 [6] Liu C-C, Feng W and Yao Y 2011 *Phys. Rev. Lett.* **107** 076802
 [7] Liu C-C, Jiang H and Yao Y 2011 *Phys. Rev. B* **84** 195430
 [8] Ezawa M 2012 *Phys. Rev. Lett.* **109** 055502
 Ezawa M 2012 *New J. Phys.* **14** 033003
 [9] Cai Y, Chuu C-P, Wei C M and Chou M Y 2013 *Phys. Rev. B* **88** 245408
 [10] Liu H, Gao J and Zhao J 2013 *J. Phys. Chem. C* **117** 10353
 [11] Neek-Amal M, Sadeghi A, Berdiyrov G R and Peeters F M 2013 *Appl. Phys. Lett.* **103** 261904
 [12] Tahir M, Manchon A, Sabeeh K and Schwingenschlögl U 2013 *Appl. Phys. Lett.* **102** 162412
 [13] Tabert C J and Nicol E J 2013 *Phys. Rev. B* **87** 235426
 [14] Tahir M and Schwingenschlögl U 2013 *Sci. Rep.* **3** 1075
 [15] Tabert C J and Nicol E J 2013 *Phys. Rev. Lett.* **110** 197402
 [16] Hwang E H and Sarma S D 2007 *Phys. Rev. B* **75** 205418
 Wang X-F and Chakraborty T 2007 *Phys. Rev. B* **75** 033408
 [17] Ju L *et al* 2011 *Nat. Nanotechnol.* **6** 630
 [18] Kotov V N, Uchoa B, Pereira V M, Guinea F and Castro A H 2012 *Rev. Mod. Phys.* **84** 1067
 [19] Fei Z *et al* 2012 *Nature* **487** 82
 [20] Chen J *et al* 2012 *Nature* **487** 77
 [21] Tahir M and Sabeeh K 2008 *J. Phys.: Condens. Matter* **20** 425202
 [22] Roldan R, Goerbig M O and Fuchs J-N 2011 *Phys. Rev. B* **83** 205406
 [23] Goerbig M O 2011 *Rev. Mod. Phys.* **83** 1193
 [24] Wu J Y, Chen S C, Roslyak O, Gumbs G and Lin M F 2011 *ACS Nano* **5** 1026
 [25] Tymchenko M, Nikitin A Y and Moreno L M 2013 *ACS Nano* **7** 9780
 [26] Crassee I, Orlita M, Potemski M, Walter A L, Ostler M, Seyller Th, Gaponenko I, Chen J and Kuzmenko A B 2012 *Nano Lett.* **12** 2470
 [27] Yan H G, Li Z, Li X, Zhu W, Avouris P and Xia F 2012 *Nano Lett.* **12** 3766
 [28] Poumirol J M *et al* 2013 *Phys. Rev. Lett.* **110** 246803
 [29] Chang H R, Zhou J, Zhang H and Yao Y 2014 *Phys. Rev. B* **89** 201411
 [30] Tabert C J and Nicol E J 2014 *Phys. Rev. B* **89** 195410
 [31] Van Duppen B, Vasilopoulos P and Peeters F M 2014 *Phys. Rev. B* **90** 035142
 [32] Ando T 2006 *J. Phys. Soc. Japan* **75** 074716
 [33] Pyatkovskiy P K and Gusynin V P 2011 *Phys. Rev. B* **83** 075422
 [34] Gradshteyn I S and Ryzhik I M 1980 *Tables of Integrals, Series and Products* (New York: Academic)
 [35] Chiappe D, Scalise E, Cinquanta E, Grazianetti C, Broek B v, Fanciulli M, Houssa M and Molle A 2014 *Adv. Mater.* **26** 2096
 [36] Peres N M R and Castro E V 2007 *J. Phys.: Condens. Matter* **19** 406231
 Lukose V, Shankar R and Baskaran G 2007 *Phys. Rev. Lett.* **98** 116802
 Krstajić P and Vasilopoulos P 2011 *Phys. Rev. B* **83** 075427